JACS
JOURNAL OF THE AMERICAN CHEMICAL SOCIETY
Article
pubs.acs.org/JACS

Iron L-Edge X-ray Absorption Spectroscopy of Oxy-Picket Fence Porphyrin: Experimental Insight into Fe−O_2 Bonding

Samuel A. Wilson,[†] Thomas Kroll,[†] Richard A. Decreau,[†,§] Rosalie K. Hocking,[†,⊥] Marcus Lundberg,[†,∥] Britt Hedman,*[,‡] Keith O. Hodgson,*[,†,‡] and Edward I. Solomon*[,†,‡]

[†]Department of Chemistry, Stanford University, Stanford, California 94305, United States

[‡]Stanford Synchrotron Radiation Lightsource, SLAC National Accelerator Laboratory, Stanford University, Menlo Park, California 94025-7015, United States

Supporting Information

ABSTRACT: The electronic structure of the Fe−O_2 center in oxy-hemoglobin and oxy-myoglobin is a long-standing issue in the field of bioinorganic chemistry. Spectroscopic studies have been complicated by the highly delocalized nature of the porphyrin, and calculations require interpretation of multi-determinant wave functions for a highly covalent metal site. Here, iron L-edge X-ray absorption spectroscopy, interpreted using a valence bond configuration interaction multiplet model, is applied to directly probe the electronic structure of the iron in the biomimetic Fe−O_2 heme complex [Fe(pfp)-(1-MeIm)O_2] (pfp ("picket fence porphyrin") = *meso*-tetra(*α,α,α,α-o*-pivalamidophenyl)porphyrin or TpivPP). This method allows separate estimates of *σ*-donor, *π*-donor, and *π*-acceptor interactions through ligand-to-metal charge transfer and metal-to-ligand charge transfer mixing pathways. The L-edge spectrum of [Fe(pfp)(1-MeIm)O_2] is further compared to those of [Fe^{II}(pfp)(1-MeIm)$_2$], [Fe^{II}(pfp)], and [Fe^{III}(tpp)(ImH)$_2$]Cl (tpp = *meso*-tetraphenylporphyrin) which have Fe^{II} S = 0, Fe^{II} S = 1, and Fe^{III} S = 1/2 ground states, respectively. These serve as references for the three possible contributions to the ground state of oxy-pfp. The Fe−O_2 pfp site is experimentally determined to have both significant *σ*-donation and a strong *π*-interaction of the O_2 with the iron, with the latter having implications with respect to the spin polarization of the ground state.

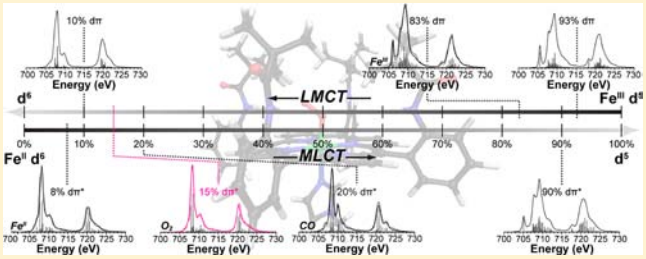

1. INTRODUCTION

Oxy-hemoglobin (Hb) and oxy-myoglobin (Mb) are dioxygen transport and storage metalloproteins located in red blood cells and aerobic muscle tissue.[1−4] Both of these proteins feature an iron heme active site in which the deoxygenated form has a high-spin (S = 2) ferrous center that becomes diamagnetic upon O_2 binding.[5,6] While the end-on Fe−O_2 geometric structures of Hb and Mb are well known,[7−9] there has been a long-standing discussion, recently summarized by Shaik et al.,[10] concerning the electronic structure of the Fe−O_2 bond. Three limiting descriptions of the Fe−O_2 bond have generally been considered: a low-spin (S = 0) ferrous center with singlet O_2, as initially suggested by Pauling;[6,11] a low-spin (S = 1/2) ferric center, antiferromagnetically coupled to an O_2^- doublet, as proposed by Weiss;[12] and an intermediate-spin (S = 1) ferrous site, antiferromagnetically coupled to triplet O_2, referred to as the ozone model of McClure, Harcout, and Goddard (Scheme 1).[13−16]

An array of different spectroscopic and computational methods have been used in attempts to address the nature of the Fe−O_2 bond in Hb and Mb.[3,10,17−29] The heme unit is highly covalent, with significant delocalization of the iron 3d electrons into the porphyrin π^* system.[29−35] The ability of the heme to redistribute the charge and spin density of the iron plays an essential role in the formation and stabilization of a variety of intermediates required for biological function.[36] However, this delocalization also complicates the ability of many spectral methods to evaluate the electronic structure of the iron.[37] Furthermore, the presence of several energetically accessible spin states can make computational evaluations challenging.[22−26]

Scheme 1. The Three Limiting Descriptions of the Fe−O_2 Bond[a]

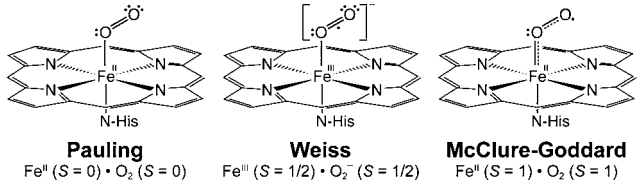

[a]Left to right: Pauling low-spin (S = 0) Fe^{II} singlet with singlet O_2; Weiss low-spin (S = 1/2) Fe^{III} doublet, antiferromagnetically coupled to an O_2^- doublet; and the McClure, Harcout, and Goddard intermediate-spin (S = 1) Fe^{II} triplet, antiferromagnetically coupled to triplet O_2 (ozone model).

Received: October 24, 2012
Published: December 22, 2012

dx.doi.org/10.1021/ja3103583 | J. Am. Chem. Soc. 2013, 135, 1124−1136

Iron L-edge X-ray absorption spectroscopy (XAS) directly focuses on the electronic structure of a metal center in a highly covalent environment, as in a porphyrin.[37] The L-edge spectrum involves an electric dipole-allowed 2p→3d transition, and since the 2p orbital is localized on the iron, the intensity of the L-edge quantifies the amount of metal d-character in the unoccupied valence orbitals of the complex.[38] As unoccupied d-character (i.e., L-edge intensity) increases or decreases, the Z_{eff} of the iron changes accordingly, as does the energy of the L-edge transition. Ligand donor interactions through ligand-to-metal charge transfer (LMCT) configuration interaction (CI) decrease the amount of d-character, while ligand acceptor interactions through metal-to-ligand charge transfer (MLCT) backbonding shift occupied metal character into the ligand π^* orbitals, which results in increased L-edge intensity.[37,39]

The iron L-edge spectrum is split into two main spectroscopic features. These arise from the presence of a 2p core hole which has a large spin-orbit interaction that gives the L_3 (J = 3/2) and L_2 (J = 1/2) peaks. These peaks are energy-split by ∼10−15 eV with an intensity ratio of ∼2:1. Furthermore, the 2p→3d transitions produce $2p^5 3d^{N+1}$ final states that are split in energy by p-d and d-d electron repulsion and ligand field effects. In the low-spin iron heme systems studied here, the ligand field splitting is large and separates the dπ from the dσ holes by several electronvolts. To these are added the differential orbital covalency (DOC),[38] the difference in covalency for the dπ and dσ levels, which influences the intensity pattern of the final state multiplets. Note that in heme systems the σ-covalency in D_{4h} further splits into a_{1g} (d_{z^2}) and b_{1g} ($d_{x^2-y^2}$) components. Thus, covalency affects both the L-edge intensity and its distribution. This is included in the analysis of the L-edge spectrum through LMCT CI for donation and MLCT CI for backbonding.

In this investigation, iron L-edge XAS is used to study oxy-picket fence porphyrin[7,40] (pfp = *meso*-tetra(α,α,α,α-*o*-pival-amido-phenyl)porphyrin, or TpivPP), the first structurally defined reversible dioxygen binding heme complex that models Hb and Mb.[7,8] This complex exhibits similar vibrational and Mössbauer parameters to those of the proteins, and first demonstrated that dioxygen was bound to iron in an end-on fashion.[7,8] Also included are the L-edge spectra of [Fe^{II}(pfp)-(1-MeIm)$_2$] (1-MeIm = 1-methylimidazole), a low-spin (S = 0) ferrous heme complex as in the Pauling model;[6,11] ferrous [Fe^{II}(pfp)], which has no axial ligands and thus has an intermediate-spin (S = 1) as in the ozone model of McClure, Harcout, and Goddard;[13−16] [Fe^{II}(pfp)(1-MeIm)(CO)], which is a well-defined low-spin (S = 0) ferrous complex with significant π-backbonding; and [Fe^{III}(tpp)(ImH)$_2$]Cl (tpp = *meso*-tetraphenylporphyrin, ImH = imidazole), a low-spin (S = 1/2) ferric complex as considered by Weiss.[12]

This study experimentally determines the σ and π contributions to the bonding in each of these complexes. In particular we evaluate the $d_{z^2}/d_{x^2-y^2}$ dσ splitting and directly determine the dπ interaction of the iron with the π^* orbital of O_2, where in the Pauling model this bonding is innocent while in the Weiss model the spins localize on the O_2 and the iron.

2. MATERIALS AND METHODS

2.1. Samples. The compounds [Fe^{II}(pfp)(1-MeIm)$_2$], [Fe^{II}(pfp)-(1-MeIm)(CO)], [Fe(pfp)(1-MeIm)O_2], [Fe^{II}(pfp)], [Fe^{II}(tpp)-(ImH)$_2$], and [Fe^{III}(tpp)(ImH)$_2$]Cl were synthesized and characterized according to published methods.[7,40−42] Prior to data collection, all samples were maintained in a nitrogen inert atmosphere glovebox. For the L-edge measurements the samples were spread across double-sided adhesive conductive graphite tape, attached to a copper paddle, and transferred to a nitrogen glovebag for loading into the ultra-high-vacuum (UHV) experimental chamber.

2.2. XAS Data Collection and Reduction. X-ray absorption spectra were collected at the Stanford Synchrotron Radiation Lightsource on beamline 10-1 under ring operating conditions of 100−350 mA and 3 GeV. The radiation was dispersed using a spherical grating monochromator set at 1000 lines/mm with 20 μm entrance and exit slits for a resolution of ∼0.1 eV. Data for all samples were recorded using a UHV beamline end-station maintained at 5.0×10^{-9} Torr with samples aligned at 45° to the incident beam as described previously.[38,43]

L-edge spectra were measured by total electron yield with a Galileo 4716 channeltron electron multiplier aligned parallel to the sample surface normal and 45° relative to the incident beam. The signal flux (I_1) was normalized by the photocurrent of an upstream gold-grid reference monitor (I_0). The photon energy was calibrated to 708.5 and 720.1 eV for the L_3- and L_2-edges, respectively, of powdered α-Fe_2O_3 (hematite <5 μM) run before and after each set of sample scans. Data were collected over the range of 670−830 eV to allow for proper normalization,[38] with a step size of 0.1 eV employed from 700 to 730 eV, and 0.5 eV for remaining regions of the spectrum.

A single scan of the L-edge spectrum took an average of ∼10 min, with ∼4 min over the 700−730 eV energy region. Four to six scans were averaged together to obtain a final data set with a high signal-to-noise ratio. Photoreduction was only observed in the ferric reference compound [Fe^{III}(tpp)(ImH)$_2$]Cl. However, [Fe^{II}(pfp)(1-MeIm)$_2$], [Fe^{II}(pfp)(1-MeIm)(CO)], [Fe(pfp)(1-MeIm)O_2], and [Fe^{II}(tpp)-(ImH)$_2$] exhibited an increased rate of pumping decay when exposed to X-ray radiation. As a result, all samples were kept cold using a cryostat with measurements taken at temperatures between 220 and 240 K. Maintaining the samples at lower temperatures prevented decay either by pumping or photoreduction, and allowed collection of reproducible high-quality data.

A linear background function was first subtracted from each averaged data set, to which two arctangent functions of the form absorption (χ) = $\{\tan^{-1}[k(\text{energy} - I_1) + \pi/2](2/3)(1/\pi)\} + \{\tan^{-1}[k(\text{energy} - I_2) + \pi/2](1/3)(1/\pi)\}$, with k = 0.295, obtained by experimental fit,[38,44] and $I_2 = I_1 + 12.3$ eV (energy split by spin-orbit coupling), were used to model the L_3- and L_2-edge jumps with each set normalized to 1.0 at 830 eV as done previously.[38] The energy of the arctangent was estimated on the basis of the fit to the L-edge experiment.[37−39,45−47] For samples which exhibited degradation under UHV, pumping was minimized by rapid transfer into and out of the experimental chamber, and by maintaining the samples at or below 240 K. These data sets were corrected, following the above normalization step, by subtracting increasing percentages of a five-coordinate pumped control sample associated with each complex. The final corrected spectra were generated by subtracting increasing percentages (5%, 10%, 15%, etc.) of the pumped spectrum, followed by renormalization. When the renormalized spectrum became unphysical (negative), the limit of the possible contribution was established (see Results section). This procedure yielded a reproducible corrected spectrum for each complex.

The total intensity reported here is the combined area of the L_3 and the L_2 intensities and is calculated after normalization over the ranges of 700−715 and 715−730 eV, respectively. The error reported represents the range of integrated L-edge intensities based on at least three different background subtractions and normalizations on at least three repeat measurements of the same spectrum on different dates.

2.3. Valence Bond Configuration Interaction (VBCI) Multiplet Simulations. Ligand field multiplet calculations were performed using the multiplet model implemented by Thole,[48] with the atomic theory developed by Cowan,[49] and the crystal field symmetry interactions described by Butler,[50] which includes both Coulomb interactions and spin-orbit coupling for each subshell.[51,52] To simulate the spectra, the Slater-Condon-Shortley parameters F_i and G_i were reduced to 80% of their Hartree-Fock calculated values in order to account for the overestimation of electron-electron repulsion found in

dx.doi.org/10.1021/ja3103583 | J. Am. Chem. Soc. 2013, 135, 1124−1136

the calculations of the free ion (κ = 0.8).[51,53,54] The final multiplet spectrum is calculated from the sum of all transitions for electrons excited from an iron 2p into the 3d unoccupied orbitals.[55] In the ligand field limit, the ground state is approximated by a single electronic configuration d^N split in energy by a ligand field potential in D_{4h} symmetry, which is defined by the parameters 10Dq, Ds, and Dt. The relationships between orbital energies and ligand field parameters are b_{1g} ($d_{x^2-y^2}$) = 6Dq + 2Ds − 1Dt, a_{1g} (d_{z^2}) = 6Dq − 2Ds − 6Dt, b_{2g} (d_{xy}) = −4Dq + 2Ds − 1Dt, and e_g ($d_{xz/yz}$) = −4Dq − 1Ds + 4Dt. Covalent mixing of the valence metal d orbitals with the valence ligand p orbitals is simulated using a charge transfer model in which LMCT adds a $d^{N+1}\underline{L}$ configuration ($\underline{L}$ = ligand hole) at an energy (Δ) above the d^N ground state. These two states couple through CI, which is introduced by the mixing term $T_i = \langle 3d^N|h|d^{N+1}\underline{L}\rangle$, where h is the molecular Hamiltonian operator and T_i is proportional to the metal-ligand overlap for each of the i symmetry blocks. In the case of a donor ligand system, the ground state is defined by $\Psi_{GS,B} = \alpha_1|3d^N\rangle + \beta_1|3d^{N+1}\underline{L}\rangle$, the LMCT state is defined by $\Psi_{GS,AB} = \beta_1|3d^N\rangle - \alpha_1|3d^{N+1}\underline{L}\rangle$, and the excited states are defined as $\Psi_{ES,B} = \alpha_2|2p^53d^{N+1}\rangle + \beta_2|2p^53d^{N+2}\underline{L}\rangle$ and $\Psi_{ES,AB} = \beta_2|2p^53d^{N+1}\rangle - \alpha_2|2p^53d^{N+2}\underline{L}\rangle$. Here the coefficients α_1, α_2, β_1, and β_2 are functions of T and Δ for the ground state, and T and Δ' for the final state, where $\Delta' = \Delta + U - Q$, where U is the 3d-3d electron repulsion and Q the 2p-3d repulsion. To limit the number of variables, $Q - U$ was maintained between 1.0 and 1.2 eV.[56] Additionally, the ligand field parameters (10Dq, Ds, and Dt), T, and Δ were fixed in the ground and final state. MLCT was included by introduction of a third configuration defined as $d^{N-1}L^-$, separated from the ground state by an energy, Δ_{BB} (Δ-backbonding). The resultant ground-state wave functions are thus combinations of three configurations, $3d^{N-1}L^-$, $3d^N$, and $3d^{N+1}\underline{L}$.[37,39]

To simulate the L-edge spectra, parameters were initially chosen on the basis of previous fits[37] and constraints obtained by density functional theory (DFT) results (*vide infra*). Parameters that determine the energy separations between the $d^{N-1}L^-$, d^N, and $d^{N+1}\underline{L}$ configurations in the ground state (Δ and Δ_{BB}) were obtained from the program parameters, where EG1 = 0, EG2 = $-\Delta_{BB}$, and EG3 = $\Delta - \Delta_{BB}$, and fixed in the final state where EF1 = 0, EF2 = $-\Delta_{BB} - Q + U$, and EF3 = $\Delta - \Delta_{BB} - 2(Q - U)$.

In order to get covalency values for each of the symmetry blocks, a DOC projection method was applied that uses the multiplets[49,50] to distribute the intensity into its different symmetry components via virtual 4s→4p transitions.[38] These projected values were then degeneracy weighted and calibrated to the experimental total intensity to extract the DOC. The final simulated fit to each spectrum was evaluated on the basis of simulated spectral shape relative to the data, the relative weights of the three ground configurations ($d^{N-1}L^-$, d^N, and $d^{N+1}\underline{L}$), the projected intensities into each of the symmetry blocks, and its agreement with other spectroscopic and computational results.

2.4. DFT Calculations. The starting structures for [Fe^{II}(pfp)(1-MeIm)$_2$], [Fe^{II}(pfp)(1-MeIm)(CO)], [Fe^{II}(pfp)], and [Fe^{III}(pfp)(1-MeIm)$_2$]$^+$ were taken from, or modified from, the crystal structure of [Fe^{II}(pfp)(1-MeIm)$_2$].[57] [Fe^{II}(tpp)(ImH)$_2$] and [Fe^{III}(tpp)(ImH)$_2$]$^+$ were taken from the structure of [Fe(tpp)(ImH)$_2$]Cl.[42] [Fe(pfp)(1-MeIm)O_2] was taken directly from its crystal structure.[58]

Ground-state DFT calculations and geometry optimizations were performed with Gaussian 09[59] using the unrestricted GGA exchange functional of Becke[60] with the nonlocal correlation of Perdew[61] (UBP86) with the 6-311G* basis set on iron and the smaller 6-31G* basis set on all other atoms. Several other basis sets and functionals were tested. However, the above combination yielded results consistent with previous L-edge studies[37−39,45,47] which used UBP86 in the Amsterdam Density Functional (ADF) modeling suite.[62] Frequency calculations on the final optimized geometries contained only real frequencies. Mulliken populations were analyzed using QMForge,[63] and orbital diagrams were plotted with gOpenMol.[64,65]

3. RESULTS

L-edge X-ray absorption spectroscopy data were collected on low-spin ferrous (S = 0) [Fe^{II}(pfp)(1-MeIm)$_2$] and [Fe^{II}(pfp)(1-MeIm)(CO)], intermediate-spin (S = 1) ferrous [Fe^{II}(pfp)], low-spin ferric (S = 1/2) [Fe^{III}(tpp)(ImH)$_2$]Cl, and low-spin (S = 0) [Fe(pfp)(1-MeIm)O_2], under UHV using electron yield detection. Under these experimental conditions at room temperature, [Fe^{II}(pfp)(1-MeIm)$_2$], [Fe^{II}(pfp)(1-MeIm)(CO)], and [Fe(pfp)(1-MeIm)O_2] exhibited substantial degradation by the loss of a labile axial ligand. Thus, a control experiment was performed in which the samples were left at room temperature and pumped for one week at 5×10^{-9} Torr. For each complex, this procedure resulted in a five-coordinate pumped species with a high-spin (S = 2) L-edge spectrum. For [Fe^{II}(pfp)(1-MeIm)$_2$] this effect is shown in Figure 1 with the pumped five-coordinate species in light blue. Analogous comparisons for [Fe^{II}(pfp)(1-MeIm)(CO)] and [Fe(pfp)(1-MeIm)O_2] are given in Supporting Information (SI) Figure S1. Although the pumped data are different in both spectral shape and energy from the spectrum of interest

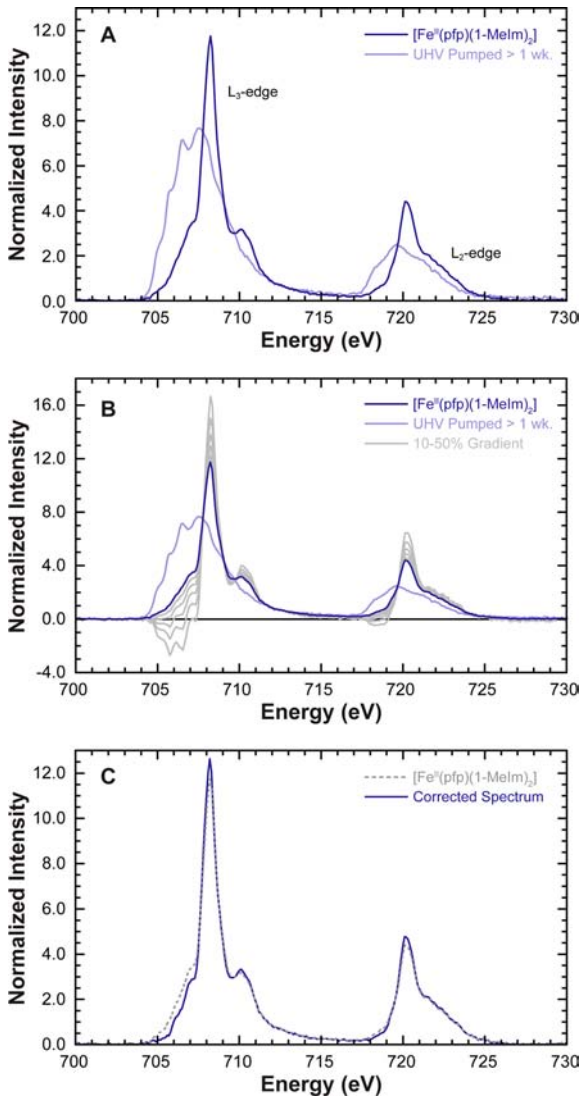

Figure 1. (A) Normalized L-edge data for [Fe^{II}(pfp)(1-MeIm)$_2$] (blue) vs the same sample pumped for one week under UHV conditions (light blue). (B) Subtraction of "pumped" data and renormalization curves (gray) from 10−50% pumped contribution. (C) Normalized L-edge data for [Fe^{II}(pfp)(1-MeIm)$_2$] (—) vs the final corrected spectrum (---) with 15% pumped contribution removed.

dx.doi.org/10.1021/ja3103583 | J. Am. Chem. Soc. 2013, 135, 1124−1136

(collected at low temperature), they do overlap the low-energy region of the $[Fe^{II}(pfp)(1\text{-MeIm})_2]$ L_3-edge, from 704 to 708 eV (Figure 1A). Therefore, the low-energy shoulder may contain a small contribution from the associated five-coordinate pumped species. A final corrected spectrum was thus generated by subtracting increasing percentages of the pumped spectrum, followed by renormalization, until the resultant spectrum became negative (unphysical, Figure 1B). This established an upper limit of contamination (Figure 1C). This procedure yielded a maximum of <15% pumped contaminant in the data for $[Fe^{II}(pfp)(1\text{-MeIm})_2]$ and $[Fe(pfp)(1\text{-MeIm})O_2]$, and <20% for $[Fe^{II}(pfp)(1\text{-MeIm})(CO)]$ (SI Figure S2).

$[Fe^{II}(pfp)(1\text{-MeIm})_2]$ is a six-coordinate low-spin (S = 0) ferrous center in the pfp ligand.[7] The L-edge spectrum of $[Fe^{II}(pfp)(1\text{-MeIm})_2]$ is similar to the L-edge spectrum of previously studied[37] $[Fe^{II}(tpp)(ImH)_2]$ (SI Figure S3) with a single main L_3 feature at 708.2 eV and a smaller high energy shoulder at 710.1 eV (Figure 1C). Together with the L_2-edge at 720.1 eV, the L-edge of $[Fe^{II}(pfp)(1\text{-MeIm})_2]$ has a total intensity of 38 normalized units, corresponding to a total metal d-character[38] of 302% in the unoccupied valence orbitals (Table 1).

Exchanging the axial 1-MeIm ligand in the picket fence cage with CO gives $[Fe(pfp)(1\text{-MeIm})(CO)]$ (Figure 2A) with the uncorrected data given in SI Figure S1.[7,8] Carbonyl (C≡O) is a strong field ligand with backbonding similar to (CN^-).[39] Compared to $[Fe^{II}(pfp)(1\text{-MeIm})_2]$, which is included as a reference in Figure 2 as the dashed line, the L_3-edge of $[Fe^{II}(pfp)(1\text{-MeIm})(CO)]$ is shifted up in energy and intensity to 708.6 eV and 41 normalized units, respectively (Table 1). The L-edge of $[Fe^{II}(pfp)(1\text{-MeIm})(CO)]$ also has substantially greater intensity in the high-energy L_3 feature at 710.0 eV relative to $[Fe^{II}(pfp)(1\text{-MeIm})_2]$, with a corresponding feature now clearly visible in the L_2-edge at 722.6 eV. These additional features result from filled metal 3d orbitals backbonding into low lying CO π^* orbitals.[39] In addition, the main L_3 feature has become narrower relative to $[Fe^{II}(pfp)\text{-}(1\text{-MeIm})_2]$, indicative of the destabilization of the d_{z^2} orbital associated with the strong σ-donor character of CO.

The L-edge spectrum of $[Fe(pfp)(1\text{-MeIm})O_2]$ (Figure 2B) is very similar to that of $[Fe^{II}(pfp)(1\text{-MeIm})_2]$ (dashed). The L_3-edge is shifted up slightly in energy (0.1 eV) to 708.3 eV compared to $[Fe^{II}(pfp)(1\text{-MeIm})_2]$, with a total intensity of 39 normalized units corresponding to 310% total d-character in the unoccupied valence orbitals. $[Fe(pfp)(1\text{-MeIm})O_2]$ also exhibits similar spectral changes as found for $[Fe^{II}(pfp)\text{-}(1\text{-MeIm})(CO)]$ (Figure 2A) with the main L_3 feature being slightly narrower than $[Fe^{II}(pfp)(1\text{-MeIm})_2]$, and with increased intensity in the high-energy feature at 710.2 eV.

The L-edge spectrum of intermediate-spin $[Fe^{II}(pfp)]$ (Figure 2C) is very different from that of the low-spin $[Fe^{II}(pfp)(1\text{-MeIm})_2]$, with a much broader low-energy L_3 peak that exhibits a unique spectral shape with three features at 705.7, 706.5, and 708.1 eV. The main 708.1 eV feature is slightly lower in energy by 0.1 eV compared to that of $[Fe^{II}(pfp)(1\text{-MeIm})_2]$, and the total intensity has increased to 40 normalized units (Table 1) representing 318% total metal d-character in the unoccupied valence orbitals. This spectral shape reflects a large energy decrease in the d_{z^2} orbital relative to the $d_{x^2-y^2}$, due to the lack of axial ligands, and additional multiplet effects as a result of the S = 1 intermediate-spin ground state (see VBCI simulations in section 4.2).

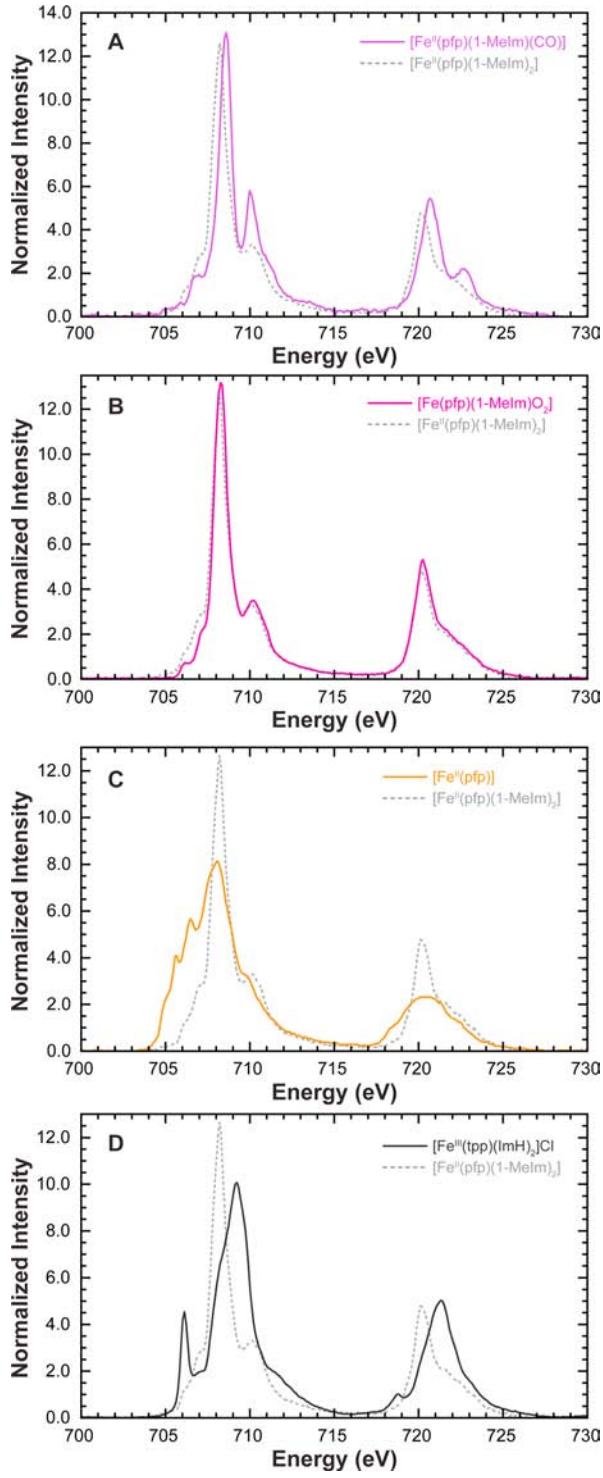

Figure 2. Corrected L-edge spectra for (A) low-spin ferrous $[Fe^{II}(pfp)(1\text{-MeIm})(CO)]$ (>20% pumped) and (B) $[Fe(pfp)\text{-}(1\text{-MeIm})(O_2)]$ (>15% pumped), (C) intermediate spin (S = 1) $[Fe^{II}(pfp)]$, and (D) low-spin ferric (S = 1/2) $[Fe^{III}(tpp)(ImH)_2]Cl$. All panels show the corrected L-edge spectrum of $[Fe^{II}(pfp)\text{-}(1\text{-MeIm})_2]$ (---) as a reference.

In pfp, an analogous low-spin (S = 1/2) ferric bis-imidazole complex, $[Fe^{III}(pfp)(1\text{-MeIm})_2]^+$, has not been well defined. Therefore, data were re-collected on $[Fe^{III}(tpp)(ImH)_2]Cl$[42] (Figure 2D) at higher resolution relative to ref 37 to compare with the higher resolution pfp spectra presented here.[37,42] Note

dx.doi.org/10.1021/ja3103583 | J. Am. Chem. Soc. 2013, 135, 1124−1136

Table 1. Summary of Iron L-Edge Experimental Data[a]

compound	total intensity	total % metal character	L_3, L_2 maxima	L_3 area	L_2 area	branching $L_3/(L_2 + L_3)$
$[Fe^{II}(pfp)(1\text{-MeIm})_2]$	38 (3)	302	708.2, 720.1	26.3	11.7	0.69
$[Fe^{III}(tpp)(ImH)_2]Cl$	46 (3)	365	709.2, 721.3	30.8	15.2	0.67
$[Fe^{II}(pfp)]$	40 (4)	318	708.1, 720.2	30.2	9.8	0.76
$[Fe^{II}(pfp)(1\text{-MeIm})(CO)]$	41 (4)	326	708.6, 720.7	27.8	13.2	0.68
$[Fe(pfp)(1\text{-MeIm})O_2]$	39 (2)	310	708.3, 720.3	26.1	12.9	0.67

[a]Total intensity is the integrated intensity of both the L_3- and L_2-edges. The total percent metal character represents the amount of d-character in the unoccupied orbitals and includes the effects of covalency and backbonding. Maxima are given in eV at the energy of the L_3- and L_2-edge.

Table 2. Calculated First Shell Bond Lengths of Picket Fence Porphyrin Complexes[a]

compound	Fe axial	Fe transaxial	Fe equatorial	Fe out-of-plane	reference
$[Fe^{II}(pfp)(1\text{-MeIm})_2]$	1.99 (2.00)	1.97 (1.99)	2.00 (1.99)	0.01 (0.00)	57
$[Fe^{III}(pfp)(1\text{-MeIm})_2]^+$	2.00	1.97	1.99	0.01	
$[Fe^{II}(pfp)]$	—	—	1.98	0.00	
$[Fe^{II}(pfp)(1\text{-MeIm})(CO)]$	1.73	2.06	2.01	0.05	
$[Fe^{II}(tpp)(ImH)_2]$	1.97	1.97	2.00	0.00	
$[Fe^{III}(tpp)(ImH)_2]^+$	1.98 (1.96)	1.98 (1.96)	2.01 (1.99)	0.00 (0.00)	42

[a]First shell bond lengths (Å) of geometry optimized structures (UPB86 with 6-311G* on Fe, 6-31G* on C, N, O, H). Measurements compared to crystal structure geometries, in parentheses, where available. Fe axial refers to the picket substituted side of the porphyrin. Fe equatorial is an average of the four Fe−N heme bonds.

that the L-edge spectra of $[Fe^{II}(pfp)(1\text{-MeIm})_2]$ and $[Fe^{II}(tpp)(ImH)_2]$ are essentially equivalent (SI Figure S3), and therefore $[Fe^{III}(tpp)(ImH)_2]Cl$ serves as a reasonable reference. Relative to $[Fe^{II}(pfp)(1\text{-MeIm})_2]$, the L-edge spectrum of $[Fe^{III}(tpp)(ImH)_2]Cl$ is shifted to higher energy by 1.0 eV with a maximum at 709.2 eV and an increase in the total intensity to 46 normalized units, or 365% metal d-character in the unoccupied valence orbitals, both of which reflect the increase in Z_{eff} of a ferric relative to a ferrous complex. However, the most noticeable difference is the formation of the prominent low-energy feature at 706.1 eV. This feature has been assigned as the 2p transition to the 3d t_2^5 dπ hole[37−39] and is a clear characteristic feature of a low-spin ferric species. It is important to note that $[Fe(pfp)(1\text{-MeIm})O_2]$ (Figure 2B) lacks this feature in its L-edge XAS spectrum (SI Figure S4).

4. ANALYSIS

4.1. DFT Calculations of Reference Complexes. DFT calculations on $[Fe^{II}(pfp)(1\text{-MeIm})_2]$, $[Fe^{II}(pfp)(1\text{-MeIm})(CO)]$, $[Fe^{II}(pfp)]$, and $[Fe^{III}(pfp)(1\text{-MeIm})_2]^+$ are presented here for correlation to the VBCI modeling (section 4.2) of the spectra in Figures 1 and 2.

4.1.1. Geometric Structures. Calculations were performed starting from the crystal structure of low-spin (S = 0) ferrous $[Fe^{II}(pfp)(1\text{-MeIm})_2]$.[7,57] Geometry optimization did not appreciably alter the geometric or electronic structure of this complex (Table 2). Geometry optimized models for low-spin (S = 0) ferrous $[Fe^{II}(pfp)(1\text{-MeIm})(CO)]$, low-spin ferric ($S$ = 1/2) $[Fe^{III}(pfp)(1\text{-MeIm})_2]^+$, and intermediate-spin (S = 1) $[Fe^{II}(pfp)]$ were generated from the crystal structure of $[Fe^{II}(pfp)(1\text{-MeIm})_2]$ by exchanging the axial 1-MeIm ligand with CO or by removing both axial ligands generating a four-coordinate complex. For reference, first shell optimized bond lengths of $[Fe^{II}(tpp)(ImH)_2]$ and $[Fe^{III}(tpp)(ImH)_2]^+$ are also provided in Table 2, and SI Figure S5 shows a comparison with previous results to describe any difference between heme bonding in the pfp and tpp ligands.[37]

The first shell bond lengths of all optimized structures along with crystallographic distances are given in Table 2. In tpp, the creation of the dπ hole in the ferric complex results in increased donation from the heme ring[37] and a slight elongation (0.01 Å) in the equatorial and axial Fe−imidazole bonds. However, in pfp, the steric bulk of the pickets results in asymmetric axial bond lengths, with the longer bond in the sterically constrained picket cage. In addition, the steric interactions of the pickets causes a slight ruffling of the heme in pfp, relative to tpp which is planar, and can be seen in the out-of-plane distances for the iron atom. Exchanging the axial 1-MeIm for a carbonyl group results in the largest structural change of any pfp complex with a short 1.73 Å axial Fe−CO bond. This short bond results in a significant trans effect with a long 2.06 Å axial Fe−imidazole bond. The short CO bond also produces longer equatorial bonds due to the weaker Fe−heme interactions with the donut of the d_{z^2} orbital. The opposite occurs for the four-coordinate complex, which exhibits the shortest equatorial bonds of any pfp complex at an average of 1.98 Å (Table 2).

4.1.2. Electronic Structures. Figure 3 shows the energy levels, orbital contours, and the decomposition of the orbital fragments from a Mulliken population analysis of $[Fe^{II}(pfp)(1\text{-MeIm})_2]$, $[Fe^{II}(pfp)(1\text{-MeIm})(CO)]$, $[Fe^{III}(pfp)(1\text{-MeIm})_2]^+$, and $[Fe^{II}(pfp)]$ from left to right, respectively, with those of $[Fe^{II}(tpp)(ImH)_2]$ and $[Fe^{III}(tpp)(ImH)_2]^+$ given in SI Figure S5.

The molecular orbital diagram of $[Fe^{II}(pfp)(1\text{-MeIm})_2]$ is very similar to that reported for $[Fe^{II}(tpp)(ImH)_2]$[37] with two main sets of Fe d orbitals, the unoccupied b_{1g} $d_{x^2-y^2}$ {335} and a_{1g} d_{z^2} {329} (referenced to D_{4h} symmetry), with the occupied e_g d_{xz} {323}, d_{yz} {324}, and b_{2g} d_{xy} {325} lower in energy (Figure 3, left). In between these sets of 3d orbitals are the approximately degenerate low-lying unoccupied porphyrin π^* orbitals {326 and 327} which contain some (10%) iron d_{xz} and d_{xy} character, due to backbonding. Similar to tpp,[37] the $d_{x^2-y^2}$ molecular orbital is highest in energy indicating that the porphyrin is a stronger σ-donor relative to 1-MeIm. However, there is a greater amount of metal character in both the $d_{x^2-y^2}$ and the d_{z^2} orbital, 68% vs 66% and 69% vs 66%, respectively,

dx.doi.org/10.1021/ja3103583 | J. Am. Chem. Soc. 2013, 135, 1124−1136

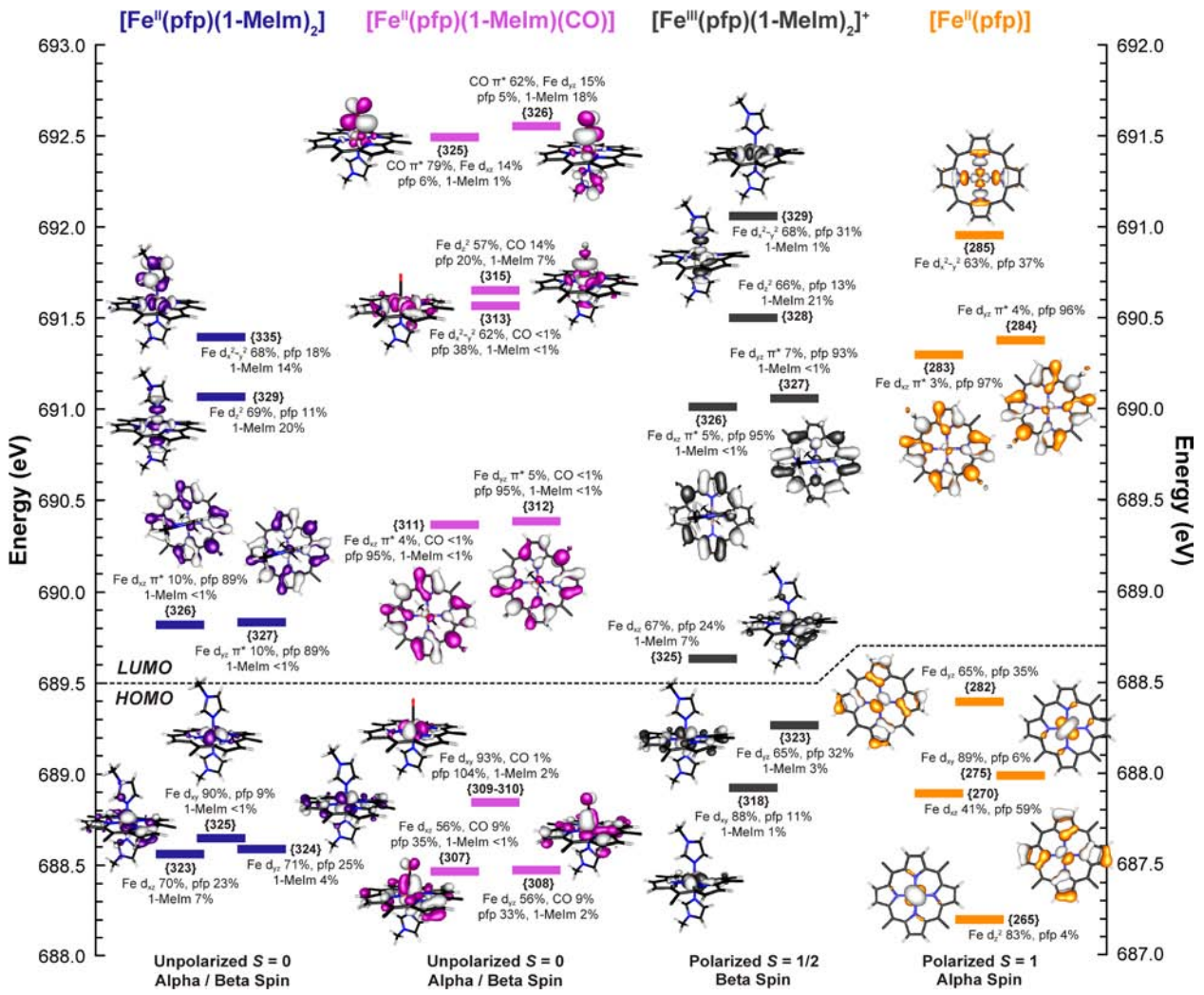

Figure 3. Comparison of the molecular orbitals for low-spin $[Fe^{II}(pfp)(1\text{-MeIm})_2]$ (blue), $[Fe^{II}(pfp)(1\text{-MeIm})(CO)]$ (purple), and $[Fe^{III}(pfp)(1\text{-MeIm})_2]^+$ (black) plotted on the left energy axis, with intermediate-spin (S = 1) ferrous $[Fe^{II}(pfp)]$ (orange) on the right axis. Orbitals are numbered according to the Gaussian output with the predominant fragment components in each molecular orbital listed above or below. Energy axes are shifted with the lowest energy Fe 2p orbital set to zero. For reference, the complete α and β molecular orbitals of $[Fe^{III}(pfp)(1\text{-MeIm})_2]^+$ and $[Fe^{II}(pfp)]$ are given in SI Figure S6. The picket porphyrin substituents have been removed for clarity but were included in all calculations. Orbitals are plotted with an isodensity value of $\pm$ 0.03.

for pfp relative to tpp (SI Figure S5). This indicates that the σ-donation into the $d_{x^2-y^2}$ and d_{z^2} orbitals from the heme and imidazole in the pfp complex(s) is not as strong as in tpp, consistent with the heme ruffling and the longer axial bonds described above.

In $[Fe^{II}(pfp)(1\text{-MeIm})(CO)]$, the carbonyl is a stronger field ligand compared to 1-MeIm. As suggested by its short 1.73 Å Fe−CO bond, the strong σ-donation of the CO lone pair destabilizes the d_{z^2} orbital {315} to higher energy relative to the other d orbitals (Figure 3). This shift is accompanied by a decrease in metal character in the d_{z^2} orbital from 69% to 57% for $[Fe^{II}(pfp)(1\text{-MeIm})(CO)]$ relative to $[Fe^{II}(pfp)(1\text{-MeIm})_2]$. The CO also adds an additional set of low-lying CO π^* orbitals {325 and 326} above the 3d σ orbitals. These CO π^* orbitals contain some metal d-character from the d_{xz} {307} and d_{yz} {308} orbitals, calculated at ~15%. The backbonding into the CO π^* orbitals decreases the amount of backbonding into the porphyrin π^* orbitals {311 and 312} which now contain only half (~5%) the metal character compared to those of $[Fe^{II}(pfp)(1\text{-MeIm})_2]$. Thus, CO is a stronger backbonding ligand than the porphyrin. While not directly impacting the L-edge, the calculations show that this increase in backbonding also stabilizes the $d_{xz/yz}$ set, resulting in a larger splitting between the occupied $d_{xz/yz}$ and d_{xy} orbitals (Figure 3). However, the L-edge transitions into the CO π^* orbitals can be directly observed in the spectrum as the intense high-energy peak on the L_3- and L_2-edge at 710.0 and 722.6 eV, respectively (*vide infra*, Figure 2A).

For the low-spin (S = 1/2) ferric complex $[Fe^{III}(pfp)(1\text{-MeIm})_2]^+$, the additional hole in the d_{xz} orbital allows π-donation from the occupied porphyrin π orbitals into the dπ-hole reducing the calculated metal d-character in the d_{xz} orbital {325} from 70% to 67% relative to $[Fe^{II}(pfp)(1\text{-MeIm})_2]$ (Figure 3). This also results in a decrease in backbonding into the porphyrin π^* orbitals, from 10% to 6% {326 and 327} for $[Fe^{II}(pfp)(1\text{-MeIm})_2]$ to $[Fe^{III}(pfp)(1\text{-MeIm})_2]^+$, respectively. This is similar to that observed for $[Fe^{III}(tpp)(ImH)_2]^+$ relative to $[Fe^{II}(tpp)(ImH)_2]^+$ (SI Figure S5).[37] Additionally, the longer axial bond in $[Fe^{III}(pfp)(1\text{-MeIm})_2]^+$ (Table 2) stabilizes the d_{z^2} orbital, and results in a ~0.5 eV increase in

dx.doi.org/10.1021/ja3103583 | J. Am. Chem. Soc. 2013, 135, 1124−1136

Table 3. Final VBCI Fit Parameters[a]

compound	crystal field	configuration energies			mixing parameters (T)				
	10Dq, Ds, Dt	Δ	Δ_{BB}	$Q-U$	x^2-y^2 (b_{1g})	z^2 (a_{1g})	xy (b_{2g})	xz/yz (e_g)	xz/yz (π^*)
$[Fe^{II}(pfp)(1\text{-MeIm})_2]$	2.40, 0.09, 0.07	−0.60	−1.65	1.2	2.15	1.80	0.50	1.50	0.65
$[Fe^{III}(tpp)(ImH)_2]^+$	2.65, 0.09, 0.08	−0.60	−1.00	1.2	2.85	2.50	1.00	1.50	1.00
$[Fe^{II}(pfp)]$	2.30, 0.40, 0.10	−0.60	−0.60	1.2	2.15	0.50	0.50	0.85	0.20
$[Fe^{II}(pfp)(1\text{-MeIm})(CO)]$	2.50, 0.15, 0.02	−1.60	−2.90	1.0	2.15	2.25	0.50	2.80	1.80
$[Fe(pfp)(1\text{-MeIm})O_2]$	2.40, 0.09, 0.05	−1.80	−2.25	1.1	2.15	1.95	0.50	2.10	1.00

[a]Final fit parameters for the $2p^6$ initial state and $2p^5$ final state with a d^6 ground state configuration. b_{1g}, a_{1g}, b_{2g}, and e_g represent LMCT mixing parameters, and π^* represents MLCT mixing. All other MLCT T values were set to zero.

Table 4. Comparison of Calculated and Experimental d Characters in Valence Orbitals for Reference Complexes[a]

compound	TI	total % metal character			VBCI (DFT) % metal character per orbital (DOC)				
		intensity	VBCI	DFT	x^2-y^2 (b_{1g})	z^2 (a_{1g})	xy (b_{2g})	xz/yz (e_g)	xz/yz (π^*)
$[Fe^{II}(pfp)(1\text{-MeIm})_2]$	38 (3)	302	306	314	68 (68)	69 (69)	(90)	(71)	8 (10)
$[Fe^{III}(tpp)(ImH)_2]^+$	46 (3)	365	361	363	68 (67)	63 (67)	(90)	83 (71)	4 (6)
$[Fe^{II}(pfp)]$	40 (4)	318	318	316	69 (67)	85 (83)	(90)	71 (83)	6 (4)
$[Fe^{II}(pfp)(1\text{-MeIm})(CO)]$	41 (4)	326	328	314	64 (62)	60 (57)	(93)	(56)	20 (19)

[a]The percent metal character summed over the unoccupied orbitals reflects the combined effects of covalency and backbonding. TI = total intensity from the integrated L-edge spectrum. The projected VBCI values for each orbital symmetry are given along with the corresponding DFT values, where values for d_{xz}, d_{yz}, and π^* orbitals are averaged for both α and β spins to compare to the VBCI model in D_{4h} symmetry.

energy splitting between d_{z^2} {328} and $d_{x^2-y^2}$ {329} orbital for both the α and β spins, as compared to $[Fe^{II}(pfp)(1\text{-MeIm})_2]$, despite the ~3% increase in covalency in the d_{z^2} orbital.

In $[Fe^{II}(pfp)]$, the lack of axial ligands results in a large stabilization of the d_{z^2} orbital and an intermediate-spin $S = 1$ ground state with two α electrons and two β holes in the d_{z^2} and d_{xz} orbitals (Figure 3, right and SI Figure S6). The occupied α d_{z^2} orbital {265} has been shifted below the HOMO/LUMO gap, and with no axial ligands the amount of metal character in the d_{z^2} orbital has increased from 69% to 83% in $[Fe^{II}(pfp)]$ relative to $[Fe^{II}(pfp)(1\text{-MeIm})_2]$ (Figure 3, right). The presence of the β hole in the d_{xz} also allows for π-donation from the heme, resulting in an average of 83% metal character in the $d_{xz/yz}$ orbitals (SI Figure S6), and a decrease in π-backbonding to ~4% {α 283 and 284}, similar to that found for the low-spin ferric heme complexes.[37]

4.2. VBCI Modeling of Reference Complexes. Based on the above DFT calculations which indicate only small differences in the heme bonding interactions between tpp and pfp, the iron L-edge of $[Fe^{II}(pfp)(1\text{-MeIm})_2]$ was simulated starting from the previous fit to $[Fe^{II}(tpp)(ImH)_2]$.[37] VBCI fitting was done using an iterative approach by first taking into account ligand field effects followed by covalency contributions, maintaining the same T, Δ, and Δ_{BB} parameters for the ground and final states. The final multiplet fit to $[Fe^{II}(pfp)(1\text{-MeIm})_2]$ is presented in Figure 4, with fit parameters given in Table 3. For reference, VBCI fits to the uncorrected L-edge data are also given in SI Figure S7. This fit yielded projected differential orbital covalencies (DOC) of 68%, 69%, and 8%, metal character in the unoccupied $d_{x^2-y^2}$, d_{z^2}, and the porphyrin π^* orbitals, respectively (Table 4), results consistent with the DFT calculations presented in Figure 3. The multiplet fit to the L-edge spectrum of $[Fe^{II}(pfp)(1\text{-MeIm})_2]$ was used as a reference for fitting the remaining complexes.

There are four differences in the L-edge spectrum of $[Fe^{II}(pfp)(1\text{-MeIm})(CO)]$ relative to that of $[Fe^{II}(pfp)(1\text{-MeIm})_2]$ (Figure 2A). The first is a sharpening of the L_3-edge which was simulated by an increase in the energy of the d_{z^2} orbital by a decrease in Dt and by an increase in the σ-LMCT mixing through T (a_{1g}). These changes reflect the strong σ-donation of the CO. The second is the additional high-energy feature at 710.0 eV (Figure 2A) which was accounted for by an increase in the amount of MLCT from the occupied iron $d\pi$ into the CO π^* orbitals (Figure 5). The last differences are an increase in total intensity and a shift of the spectrum to higher energy. These reflect an increase in the ligand field and the unoccupied d-character in the valence orbitals (effective number of holes) due to the additional backbonding. The final fit of $[Fe^{II}(pfp)(1\text{-MeIm})(CO)]$ yields 64% metal character in b_{1g}, 60% in a_{1g}, and 20% in the π^* orbital set, with the last value reflecting contributions to both the porphyrin and the CO π^* orbitals. Based on the DFT calculation of $[Fe^{II}(pfp)(1\text{-MeIm})(CO)]$ (Figure 3), these two contributions can be separated with ~5% porphyrin and ~15% CO π^* backbonding from the iron $d_{xz/yz}$ orbital set. A final fit is presented in Figure 6, with fit parameters, projected orbital covalencies, and comparisons to DFT calculations in Tables 3 and 4.

The dominant spectroscopic differences between the six-coordinate low-spin ($S = 0$) $[Fe^{II}(pfp)(1\text{-MeIm})_2]$ and the

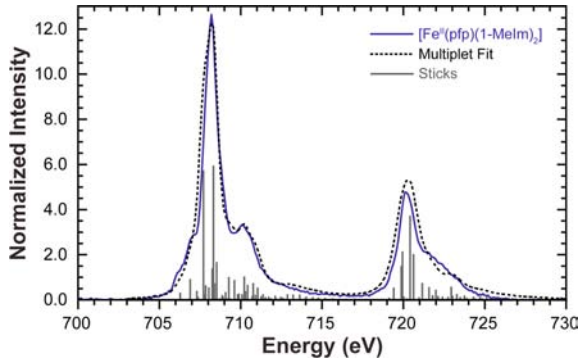

Figure 4. Final VBCI fit (---) for low-spin ferrous $[Fe^{II}(pfp)(1\text{-MeIm})_2]$. The sticks represent the individual multiplet transitions that contribute to the simulated spectrum.

dx.doi.org/10.1021/ja3103583 | J. Am. Chem. Soc. 2013, 135, 1124−1136

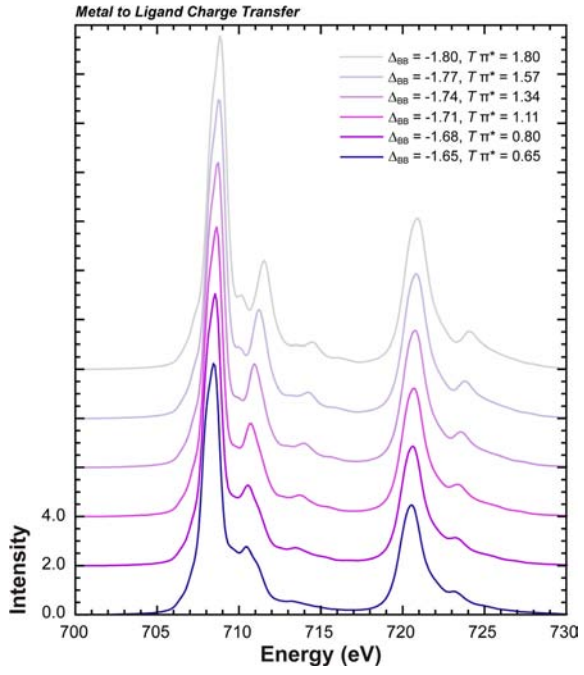

Figure 5. Systematic multiplet progression from $[Fe^{II}(pfp)(1\text{-MeIm})_2]$ to $[Fe^{II}(pfp)(1\text{-MeIm})(CO)]$ that shows the effects of increased MLCT using both Δ_{BB} and the π^* mixing parameter (T).

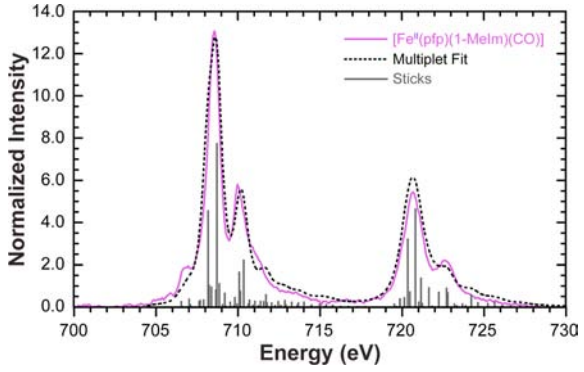

Figure 6. Final VBCI fit (---) for low-spin ferrous $[Fe^{II}(pfp)(1\text{-MeIm})(CO)]$. The VBCI multiplet fit reproduces both the sharpening of the main L_3-edge feature and the addition of the high-energy feature at 710.0 eV associated with backbonding into the CO π^* orbitals.

four-coordinate intermediate-spin (S = 1) $[Fe^{II}(pfp)]$ complex are the much broader L_3-edge and the unique spectral shape with three well-defined features (Figure 2C). Starting from $[Fe^{II}(pfp)(1\text{-MeIm})_2]$, these spectral changes were simulated by adjusting the ligand field parameters 10Dq, Ds, and Dt to stabilize the d_{z^2} orbital relative to the d-manifold (Figure 7). This results in a discontinuity (∗) in the L-edge progression where the ground state changes from a low-spin S = 0 to an intermediate-spin S = 1 once the d_{z^2} orbital is low enough in energy to depopulate one dπ electron from the filled subshell of the S = 0 $[Fe^{II}(pfp)(1\text{-MeIm})_2]$ complex. This spin state change results in the spectral broadening and the three-peak multiplet structure observed in the L-edge spectrum. To generate a final VBCI fit for the four-coordinate $[Fe^{II}(pfp)]$ complex (Figure 8), LMCT and MLCT parameters were adjusted to decrease σ-donation into the a_{1g}, and π-backbonding into the porphyrin π^* orbitals, relative to $[Fe^{II}(pfp)(1\text{-MeIm})_2]$ (Table 3). This produced an increase in metal character from 69% to 85% in the d_{z^2} orbital (Table 4), as observed in the DFT calculations, and reflects the loss of the axial ligands.

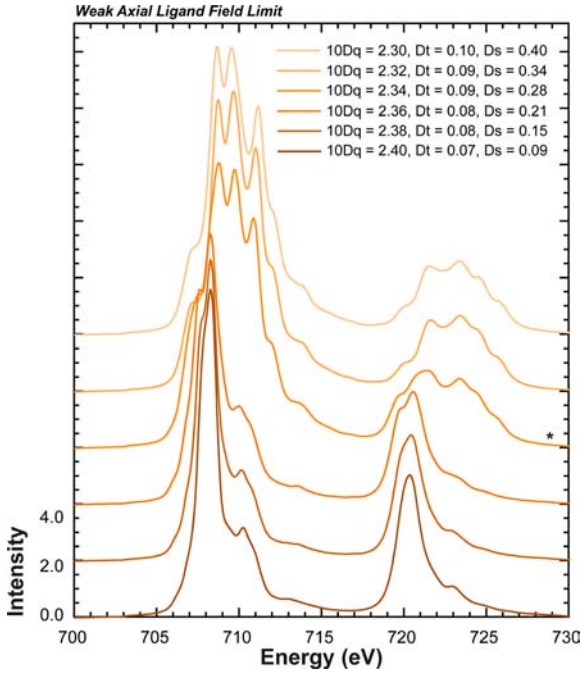

Figure 7. Systematic multiplet progression from low-spin (S = 0) $[Fe^{II}(pfp)(1\text{-MeIm})_2]$ to intermediate-spin (S = 1). The spin state change occurs between traces three and four, orange (∗), and results in the observed spectral broadening and three peak multiplet structure observed for $[Fe^{II}(pfp)]$.

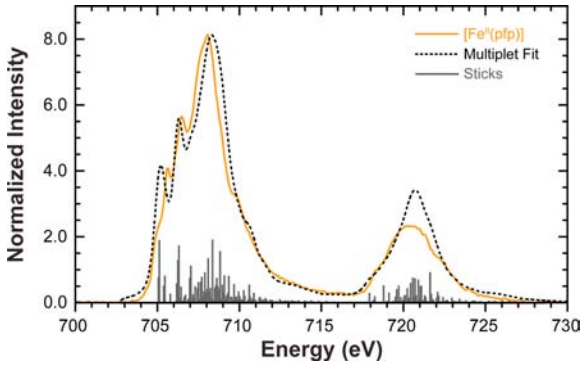

Figure 8. Final VBCI fit (---) for intermediate-spin (S = 1) ferrous four-coordinate $[Fe^{II}(pfp)]$. The VBCI multiplet fit reproduces both the broadening of the main L_3-edge feature and the relative three feature L_3-edge structure.

The higher resolution L-edge data of low-spin ferric (S = 1/2) $[Fe^{III}(tpp)(ImH)_2]Cl$ (Figure 2D) were refit as described above using the same T, Δ, and Δ_{BB} parameters for the ground and final states relative to ref 37 (Figure 9). The resulting fit parameters (Table 3) reproduce the previous study,[37] where the presence of the dπ hole allows for 17% π-donation from the heme and decreases the amount of MLCT backbonding into the porphyrin π^* orbitals from 8% to 4% relative to $[Fe^{II}(pfp)(1\text{-MeIm})_2]$.

4.2.1. Oxy-Picket Fence Porphyrin: VBCI Modeling of L-Edge XAS. To quantitatively analyze the L-edge spectrum of oxy-pfp, $[Fe(pfp)(1\text{-MeIm})O_2]$ (Figure 2B), two series of

dx.doi.org/10.1021/ja3103583 | J. Am. Chem. Soc. 2013, 135, 1124−1136

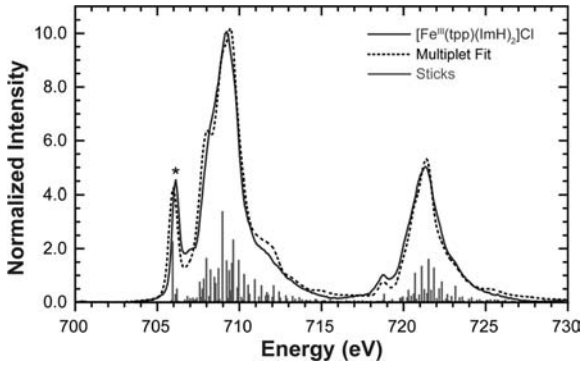

Figure 9. L-edge fit (---) to low-spin (S = 1/2) ferric [Fe^{III}(tpp)-($ImH)_2$]Cl. This fit reproduces the previous result[37] on low-spin ferric heme complexes where the presence of a dπ hole (∗) increases the amount of π-donation from the heme and reduces the amount of MLCT backbonding into the porphyrin π* orbitals.

systematic simulations were evaluated starting from both the ferrous and ferric limits of the VBCI model (Figure 10). From the fit parameters of [Fe^{II}(pfp)(1-MeIm)$_2$] (Table 3), the energy of the MLCT d^{N-1} configuration, π* Δ_{BB}, was systematically decreased from −1.65 to −8.65 eV in steps of 0.64 eV. The fit of [Fe^{II}(pfp)(1-MeIm)$_2$] (the low-spin d^6 reference) is given by the first trace, A, in Figure 10, left. Note, this simulation differs from that in Figure 4 due to an increase in the ligand field required to maintain the low-spin configuration throughout this series (i.e., the spin pairing energy is higher for a ferric relative to a ferrous complex, SI Figure S8). Throughout the progression, each trace was projected and the amount of backbonding quantified in terms of its dπ* character.

As the backbonding is increased (i.e., the energy of Δ_{BB} is decreased and becomes dominant), the ratio of the d^N (d^6) relative to the $d^{N-1}L^-$ (d^5) configuration changes and more charge is transferred from the iron dπ orbitals to the O_2 through MLCT mixing. Between Δ_{BB} = −4.20 and −4.83 eV the d^{N-1} configuration becomes dominant, trace B, and the dπ hole starts to appear in the lower energy region of the simulated spectrum (∗). This feature in the iron L-edge is characteristic of a low-spin ferric contribution, where the intensity in this peak is proportional to the amount of π-backbonding into O_2 from the iron dπ orbitals. At Δ_{BB} = −6.74 eV, trace C, the amount of dπ* character is 84%, similar to the amount of dπ hole character in the low-spin ferric heme reference [Fe^{III}(tpp)-($ImH)_2$]Cl (Figure 9 and Table 4). As Δ_{BB} is further decreased, the simulation approaches a pure low-spin d^5 state, with the final trace, D, at 90% dπ* hole at Δ_{BB} = −8.65 eV.

Starting from the final fit parameters of [Fe^{III}(tpp)($ImH)_2$]Cl as a low-spin ferric d^5 reference (trace D′ in Figure 10, right), the reverse trend is generated by systematically increasing the

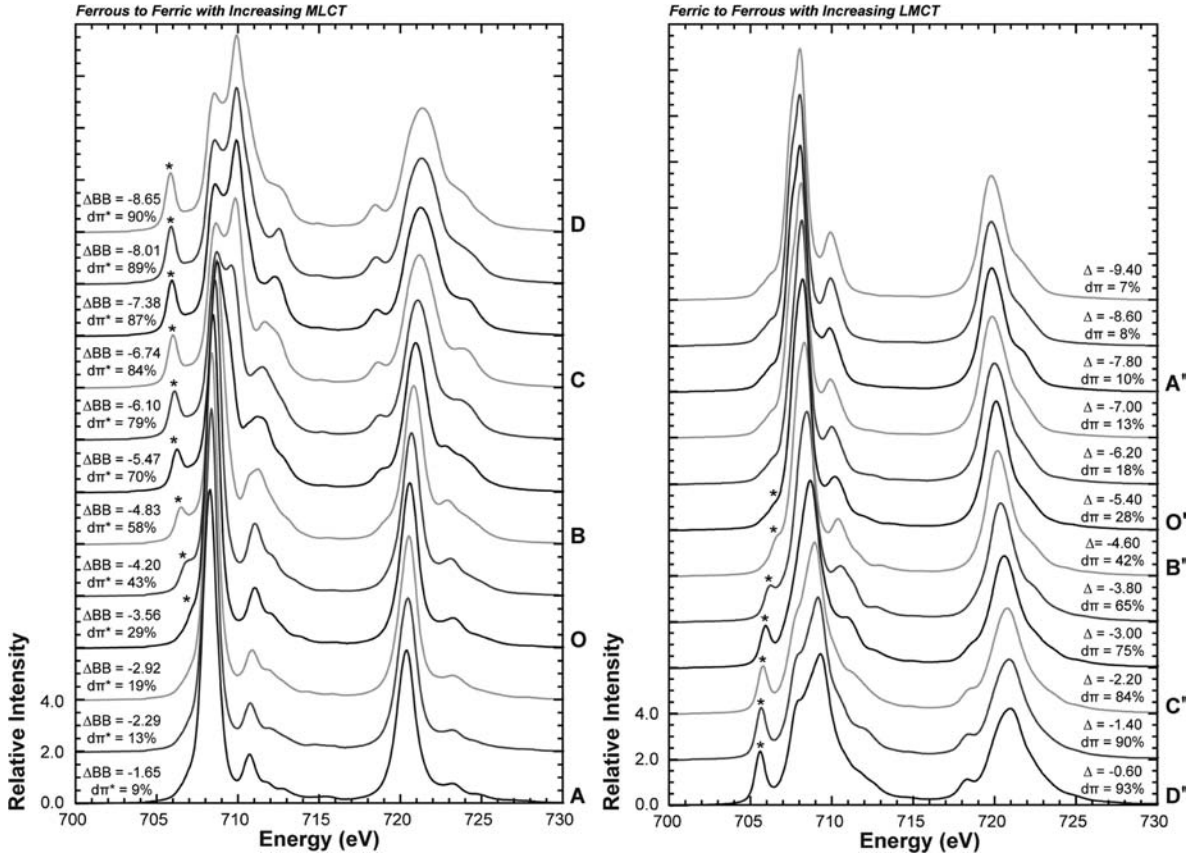

Figure 10. (Left) Systematic multiplet progression from a low-spin d^6 with Δ_{BB} = −1.65 eV to a low-spin d^5 at Δ_{BB} = −8.65 eV resulting in progressively more MLCT from 9% to 90% dπ* hole character on the iron. The first trace, A, was generated using the same parameters used to fit [Fe^{II}(pfp)(1-MeIm)$_2$], but with a larger ligand field splitting, which was required to maintain a low-spin configuration (10Dq = 3.30, Dt = 0.01). This additional progression can be found in SI Figure S8. (Right) A parallel series starting with the low-spin d^5 parameters used to fit [Fe^{III}(tpp)($ImH)_2$] Cl with progressively more LMCT into the dπ hole yielding a simulation with predominantly low-spin d^6 character. 3d spin-orbit coupling was set to zero in these simulations.

dx.doi.org/10.1021/ja3103583 | J. Am. Chem. Soc. 2013, 135, 1124−1136

Table 5. Comparison of Calculated and Experimental Values for $[Fe(pfp)(1\text{-MeIm})O_2]$[a]

		total % metal character		% metal character per orbital (DOC)				
	TI	intensity	total	x^2-y^2 (b_{1g})	z^2 (a_{1g})	xy (b_{2g})	xz/yz (e_g)	xz/yz (π^*)
$[Fe(pfp)(1\text{-MeIm})O_2]$	39 (2)	310	306	67	64	—	—	11
DFT, unpolarized	—	—	344	66	60	—	36	5
DFT, polarized (α/β)	—	—	342	65/64	62/57	—	57/11	9/4

[a]The percent metal character summed over the unoccupied orbitals reflects the combined effects of donor and backbonding. TI = total intensity from the integrated normalized L-edge spectrum. Projected VBCI orbital covalencies for $[Fe(pfp)(1\text{-MeIm})O_2]$ are from Figure 11. DFT values are based on Mulliken populations of the appropriate molecular orbitals.

O_2^- π-donation (i.e., decreasing Δ from −0.6 to −9.4 eV). Over this progression of simulations the amount of dπ hole character (peak marked with $*$ on the low-energy side of the L_3-edge) decreases as the amount of LMCT from the O_2^- to the iron dπ hole is increased. At Δ = −2.20 eV the amount of π-bonding gives a similar dπ hole character as that found for $[Fe^{III}(tpp)(ImH)_2]Cl$, trace C′. As with the progression from d^6 to d^5 (Figure 10, left), a simulated spectrum is reached at $\Delta \approx -4.60$ eV, where the d^6 configuration starts to become the main component of the wave function, trace B′, and the dπ hole spectral feature is no longer clearly distinguishable. At the end of the series (Δ = −7.80 eV) the wave function contains only ∼10% dπ hole character and the simulated spectral shape looks very similar to the iron L-edge spectrum of $[Fe^{II}(pfp)(1\text{-MeIm})_2]$, trace A′ and Figure 4.

Note that the VBCI simulation of the d^6 spectrum from a d^5 starting point has some differences from the fit presented in Figure 4, as this simulation lacks the d^{N+1} (d^7) contribution and contains some d^{N-1} (d^4) configuration. Likewise, the d^6 simulation of the d^5 $[Fe^{III}(tpp)(ImH)_2]Cl$ lacks d^{N-1} (d^4) and contains some d^{N+1} (d^7) configuration. However, both simulations do contain the dominant, d^5 and d^6, contributions to the multiplet spectrum, making the above interconversions reasonable.

Using this approach, these simulations can estimate the amount of dπ^* character in $[Fe(pfp)(1\text{-MeIm})O_2]$ as the spectral shape of $[Fe(pfp)(1\text{-MeIm})O_2]$ (Figure 2B) lacks the characteristic low-energy dπ hole feature common to low-spin ferric species (Figure 2D). Starting from the d^6 limit (Figure 10, left), increasing the amount of backbonding (MLCT) in the simulations from the dπ into O_2 gives an upper limit of 30% dπ^* character at Δ_{BB} = −3.56 eV, trace O. A similar limit is determined starting from the d^5 configuration by increasing the amount of π donation (LMCT) from the O_2^- into the iron dπ orbital. This again gives an upper limit of 30% at Δ = −5.40 eV, trace O′. These two sets of traces define $[Fe(pfp)(1\text{-MeIm})O_2]$ as having most of the π electron density at the iron, with an upper limit of 30% dπ hole character in the ground state.

A final fit to the L-edge spectrum of $[Fe(pfp)(1\text{-MeIm})O_2]$ was obtained using a d^6 ground state configuration with MLCT (d^5) and LMCT (d^7) CI (Figure 11). Projection of the fit yields values of 67%, 64%, and 11% metal d-character in the $d_{x^2-y^2}$, d_{z^2}, and dπ^* orbitals, respectively (Table 5), with fit parameters given in Table 3. This electronic structure description of $[Fe(pfp)(1\text{-MeIm})O_2]$ has the $d_{x^2-y^2}$ molecular orbital highest in energy due to the strong σ-donation from the heme, followed by the d_{z^2} orbital with strong σ-donation from dioxygen. While VBCI simulations of iron L-edge data do present a large parameter space, it can be limited through the use of well-defined reference complexes where single determinant DFT calculations can be used to identify a set of reasonable parameters. For $[Fe(pfp)(1\text{-MeIm})O_2]$, a range of final fits to the data, gave up to 15% metal character in the low-energy dπ hole (SI Figure S9). However, this combined with the simulations in Figure 10, the DFT calculations in Figure 3, and the VBCI multiplet fits to $[Fe^{II}(pfp)(1\text{-MeIm})_2]$ and $[Fe^{III}(tpp)(ImH)_2]^+$, which quantified the relative amounts of dπ hole character in each reference complex at 8% and 83%, respectively (Figures 4, 9, and S10 and Table 4), the dπ hole character in $[Fe(pfp)(1\text{-MeIm})O_2]$ is 15 ± 5%; describing $[Fe(pfp)(1\text{-MeIm})O_2]$ a having most of the dπ electron density on the iron.

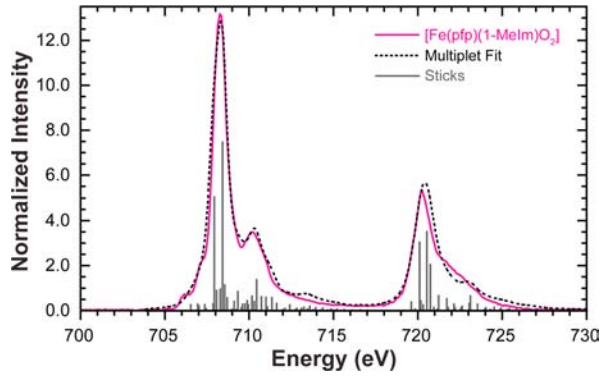

Figure 11. Final multiplet fit (---) to the L-edge spectrum of $[Fe(pfp)(1\text{-MeIm})O_2]$. Fit generated using a three-configuration (d^{N-1}, d^N, d^{N+1}) VBCI multiplet model including both MLCT and LMCT from a d^6 ground state. The sticks represent the individual multiplet transitions that contribute to the simulated spectrum.

4.2.2. Oxy-pfp: DFT of Calculations. To compare with the literature calculations of the Fe−O_2 bond in heme proteins,[10,22,24−26] DFT calculations were performed on $[Fe(pfp)(1\text{-MeIm})O_2]$ (SI Figure S11). Geometry optimization of $[Fe(pfp)(1\text{-MeIm})O_2]$ did not appreciably change the structure from that of the crystal structure[58,66] and gave first shell bond lengths and angles similar to those found in oxy-heme proteins (SI Table S1).[67,68]

These calculations gave both spin unpolarized, and spin polarized results, with the latter −2.4 kcal/mol lower in energy (SI Table S2). Both calculations gave comparable amounts of total metal character in the unoccupied valence orbitals and an appreciable amount of negative charge localized on the O_2 of $[Fe(pfp)(1\text{-MeIm})O_2]$, similar to values recently reported for DFT/MM calculations of Mb (SI Table S2).[10] Mulliken population analysis of the polarized calculation yielded 65/64% and 62/57% metal character for the $d_{x^2-y^2}$ {316} and d_{z^2} {315} α/β spin orbitals, respectively, and an average of ∼6% metal character in the porphyrin π^* orbitals {313−314} (Table 5). These values compared well to the VBCI fit to the L-edge data. Additionally, the lower energy calculation showed spin polarization of the dπ electron density with orbital {312} containing 57% d_{xz} character in the α manifold and 11% in the

dx.doi.org/10.1021/ja3103583 | J. Am. Chem. Soc. 2013, 135, 1124−1136

β (SI Figure S11). This large degree of spin polarization is not consistent with the absence of the low-energy dπ hole observed in the L-edge spectrum of [Fe(pfp)(1-MeIm)O_2] (Figure 2B), a feature characteristic of a low-spin ferric complex (Figure 2D).

5. DISCUSSION

An array of spectroscopic and computational methods have been applied to evaluate the nature of the Fe−O_2 bond in Hb and Mb.[10,17−26] In this study, iron L-edge XAS has been used to experimentally probe the electronic structure description of the Fe−O_2 center in [Fe(pfp)(1-MeIm)O_2].[7,8]

Three model complexes provide well-defined references: the low-spin (S = 0) ferrous complex, [Fe^{II}(pfp)(1-MeIm)$_2$], as in the Pauling description for the iron;[6,11] the low-spin (S = 1/2) ferric complex, [Fe^{III}(tpp)(ImH)$_2$]Cl, as in the Weiss model;[12] and an intermediate-spin (S = 1) ferrous complex, [Fe^{II}(pfp)], with one unpaired electron in the d_{z^2} and one in the d_{xz} orbital as in the McClure-Goddard-Harcourt ozone model.[13−16] To facilitate this discussion, an overlay of the L-edge data of the three reference models with that of [Fe(pfp)(1-MeIm)O_2] is presented in Figure 12. From this overlay, the L-edge spectrum of [Fe(pfp)(1-MeIm)O_2] is most similar to that of low-spin ferrous [Fe^{II}(pfp)(1-MeIm)$_2$]. However, it does exhibit some differences in multiplet structure such as a sharpening of the main L_3 feature and additional intensity on the high-energy side. This indicates that the electronic structure of the iron in the Fe−O_2 center is not simply described by any of these models, emphasizing the limitation of the three oxidation state descriptions in Scheme 1 in describing this highly covalent bond. Of the three reference complexes, the iron L-edge of [Fe^{II}(pfp)] has the least resemblance to that of [Fe(pfp)-(1-MeIm)O_2], as it exhibits a very different multiplet structure in both the L_3- and L_2-edge as well as a slight shift of 0.1 eV to lower energy, relative to [Fe^{II}(pfp)(1-MeIm)$_2$]. Compared to the low-spin ferric [Fe^{III}(tpp)(ImH)$_2$]Cl complex, the L-edge spectrum of [Fe(pfp)(1-MeIm)O_2] is also significantly different as it does not exhibit the signature low-energy peak associated with the dπ hole.

Analysis of the L-edge data on [Fe(pfp)(1-MeIm)O_2] (Figure 12) also shows a strong σ-donation from the O_2 into the d_{z^2} orbital of the iron. This leads to a sharpening of the dominant feature in the L_3-edge relative to [Fe^{II}(pfp)-(1-MeIm)$_2$] (Figure 2B). This σ-donation, together with the strong π-interaction affects the Z_{eff} of the iron in the Fe−O_2 complex. This is measured experimentally by the total d-character in the unoccupied valence orbitals and by the energy position of the L_3-edge. In going from [Fe^{II}(pfp)(1-MeIm)$_2$] to [Fe^{II}(pfp)(1-MeIm)(CO)] to [Fe^{III}(tpp)(ImH)$_2$]Cl the energy of the L_3-edge and the intensity of the spectra increase from 708.2/38, to 708.6/41, to 709.2/46 eV/normalized units, respectively (Table 1), reflecting the increase in Z_{eff}. These same values for the L-edge of [Fe(pfp)(1-MeIm)O_2] are 708.3 eV and 39 normalized units indicating a Z_{eff} higher than that of [Fe^{II}(pfp)(1-MeIm)$_2$], but significantly lower than that of the [Fe^{III}(tpp)(ImH)$_2$]Cl complex.

From the VBCI simulations in Figure 10, starting from a low-spin ferrous limit (left side), the dπ hole in the L-edge simulation appears as the MLCT backbonding from the iron into the π^* orbital of O_2 is increased. At $\geq$30% dπ hole character in the ground state, the low-energy feature is clearly present. Alternatively, starting from the low-spin ferric limit that possesses a prominent low-energy dπ feature in the simulated

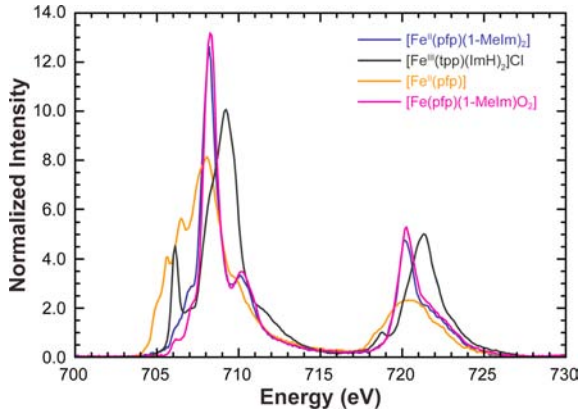

Figure 12. Overlay of the iron L-edge spectra of low-spin ferrous [Fe^{II}(pfp)(1-MeIm)$_2$] (blue), low-spin ferric [Fe^{III}(tpp)(ImH)$_2$]Cl (black), intermediate-spin ferrous [Fe^{II}(pfp)] (orange), and low-spin [Fe(pfp)(1-MeIm)O_2] (magenta).

L-edge spectrum (Figure 10), increasing the amount of LMCT from the occupied π^* orbital of O_2^- into the unoccupied dπ orbital on the iron increases the energy and decreases the intensity of this low-energy feature. With a large π-donation corresponding to $\leq$30% dπ hole character remaining in the ground state, the low-energy feature in the simulated spectrum is again no longer present, as in the iron L-edge spectrum of [Fe^{II}(pfp)(1-MeIm)$_2$]. Thus, if one starts from a Fe^{III}−O_2^- bonding description, the L-edge data of [Fe(pfp)(1-MeIm)O_2] clearly demonstrate the presence of a strong O_2^- π-donor interaction with the iron dπ orbital. As presented by Shaik,[10] the stronger the π-bonding interaction between the iron and O_2, the less spin polarization is likely to be present for the π electrons. A strong spin polarization, however, corresponds to an antiferromagnetically coupled description of the bond between the O_2 and the heme iron. Note that in pfp, there is no hydrogen bond to the distal oxygen of the Fe−O_2 site. From QM/MM calculations, this hydrogen bond is expected to play an important role in this spin polarization.[10] Thus, it will be important to compare these L-edge data and results to parallel data on Hb and Mb.

6. SUMMARY

Most spectroscopic studies of dioxygen bonding in heme systems have been complicated by the highly delocalized nature of the porphyrin, and calculations have required analysis of a multideterminant description of the highly covalent Fe−O_2 bond.[17−26] This study demonstrates both the limitations of the oxidation state formalisms for this highly covalent (both π and σ) O_2−Fe bond, and that iron L-edge XAS allows one to directly focus on the iron center in this highly covalent environment. The L-edge data of the dioxygen bond in the heme complex [Fe(pfp)(1-MeIm)O_2] do not exhibit the low-energy feature of a hole in the dπ orbital of the iron, as is characteristic of all low-spin ferric complexes.[37−39] The absence of this feature requires a strong π-interaction between the iron and the O_2 that will limit the extent of spin polarization in the Fe−O_2 bond.

■ ASSOCIATED CONTENT

Supporting Information

Additional tables, figures, multiplet fits, computational results, optimized structural coordinates, and complete ref 59. This

dx.doi.org/10.1021/ja3103583 | J. Am. Chem. Soc. 2013, 135, 1124−1136

material is available free of charge via the Internet at http://pubs.acs.org.

AUTHOR INFORMATION

Corresponding Author

hedman@slac.stanford.edu; hodgson@slac.stanford.edu; edward.solomon@stanford.edu

Present Addresses

[§]Department of Chemistry, Institut de Chimie Moléculaire, Université de Bourgogne, 21078 Dijon, France

[⊥]School of Chemistry and Monash Centre for Synchrotron Science, Clayton, 3800, Australia

[∥]Ångström Laboratory, Department of Chemistry, Uppsala University, SE-751 20 Uppsala, Sweden

Notes

The authors declare no competing financial interest.

ACKNOWLEDGMENTS

This work was supported by National Institutes of Health (NIH) grants GM 40392 (E.I.S.), 5P41RR-001209-32, and 8P41GM 103393-33 (K.O.H.), and by the National Science Foundation (NSF) grant MCB 0919027 (E.I.S.). Portions of this research were carried out at the Stanford Synchrotron Radiation Lightsource (SSRL), a Directorate of SLAC National Accelerator Laboratory and an Office of Science User Facility operated for the U.S. Department of Energy (DOE) Office of Science by Stanford University. The SSRL Structural Molecular Biology Program is supported by the DOE Office of Biological and Environmental Research and by the NIH, National Institute of General Medical Sciences (NIGMS) (including P41GM103393) and the National Center for Research Resources (NCRR) (P41RR001209). R.A.D. was supported by NIH GM-069658 to James P. Collman. T.K. thanks the German Research Foundation (DFG) grant KR3611/2. R.K.H. thanks the Monash Centre for Synchrotron Science for a Fellowship. M.L. thanks the Marcus and Amalia Wallenberg foundation for financial support.

REFERENCES

(1) Springer, B. A.; Sligar, S. G.; Olson, J. S.; Phillips, G. N., Jr.; Shikama, K. *Chem. Rev.* **1998**, *98*, 1357−1373; *Chem. Rev.* **1994**, *94*, 699−714.

(2) Dickerson, R. E.; Geiss, I. *Hemoglobin: Structure, Function, Evolution, and Pathology*; Benjamin/Cummings: Menlo Park, CA, 1983.

(3) Shikama, K. *Chem. Rev.* **1998**, *98*, 1357−1373.

(4) Perutz, M. F.; Fermi, G.; Luisi, B.; Shaanan, B.; Liddington, R. C. *Acc. Chem. Res.* **1987**, *20*, 309−321.

(5) Gamgee, A. *Proc. R. Soc. London* **1901**, *68*, 503−512.

(6) Pauling, L.; Coryell, C. D. *Proc. Natl. Acad. Sci. U.S.A.* **1936**, *22*, 210−216.

(7) Collman, J. P.; Gagne, R. R.; Reed, C. A.; Halbert, T. R.; Lang, G.; Robinson, W. T. *J. Am. Chem. Soc.* **1975**, *97*, 1427−1439.

(8) Collman, J. P.; Brauman, J. I.; Halbert, T. R.; Suslick, K. S. *Proc. Natl. Acad. Sci. U.S.A.* **1976**, *73*, 3333−3337.

(9) Shaanan, B. *J. Mol. Biol.* **1983**, *171*, 31−59.

(10) Chen, H.; Ikeda-Saito, M.; Shaik, S. *J. Am. Chem. Soc.* **2008**, *130*, 14778−14790.

(11) Pauling, L. *Nature* **1964**, *203*, 182−183.

(12) Weiss, J. J. *Nature* **1964**, *202*, 83−84.

(13) Mclure, D. S. *Res. Suppl.* **1960**, *2*, 218.

(14) Harcourt, R. D. *Int. J. Quantum Chem.* **1971**, *5*, 479−495.

(15) Harcourt, R. D. *Chem. Phys. Lett.* **1990**, *167*, 374−377.

(16) Goddard, W. A.; Olafson, B. D. *Proc. Natl. Acad. Sci. U.S.A.* **1975**, *72*, 2335−2339.

(17) Spiro, T. G.; Strekas, T. C. *J. Am. Chem. Soc.* **1974**, *96*, 338−345.

(18) Yamamoto, T.; Palmer, G.; Gill, D.; Salmeen, I. T.; Rimai, L. *J. Biol. Chem.* **1973**, *248*, 5211−5213.

(19) Marchant, L.; Sharrock, M.; Hoffman, B. M.; Münck, E. *Proc. Natl. Acad. Sci. U.S.A.* **1972**, *69*, 2396−2399.

(20) Champion, P. M.; Collins, D. W.; Fitchen, D. B. *J. Am. Chem. Soc.* **1976**, *98*, 7114−7115.

(21) Morikis, D.; Sage, J. T.; Rizos, A. K.; Champion, P. M. *J. Am. Chem. Soc.* **1988**, *110*, 6341−6342.

(22) Jensen, K. P. *J. Inorg. Biochem.* **2005**, *99*, 45−54.

(23) Jensen, K. P.; Bell, C. B. I.; Clay, M. D.; Solomon, E. I. *J. Am. Chem. Soc.* **2009**, *131*, 12155−12171.

(24) Jensen, K. P.; Roos, B. O.; Ryde, U. *J. Inorg. Biochem.* **2005**, *99*, 978.

(25) Jensen, K. P.; Ryde, U. *J. Biol. Chem.* **2004**, *279*, 14561−14569.

(26) Ribas-Ariño, J.; Novoa, J. J. *Chem. Commun.* **2007**, 3160−3162.

(27) Barlow, C. H.; Maxwell, J. C.; Wallace, W. J.; Caughey, W. S. *Biochem. Biophys. Res. Commun.* **1973**, *55*, 91−95.

(28) Spartalian, K.; Lang, G.; Yonetani, T. *Biochim. Biophys. Acta* **1976**, *428*, 281−290.

(29) Reed, C. A.; Cheung, S. K. *Proc. Natl. Acad. Sci. U.S.A.* **1977**, *74*, 1780−1784.

(30) Reynolds, C. H. *J. Org. Chem.* **1988**, *53*, 6061−6064.

(31) Yamamoto, U.; Noro, T.; Ohno, K. *Int. J. Quantum Chem.* **1992**, *42*, 1563−1575.

(32) Ghosh, A. *J. Phys. Chem. B* **1997**, *101*, 3290−3297.

(33) Lamoen, D.; Parrinello, M. *Chem. Phys. Lett.* **1996**, *248*, 309−315.

(34) Matsuzawa, N.; Ata, M.; Dixon, D. A. *J. Phys. Chem.* **1995**, *99*, 7698−7706.

(35) Loew, G. H.; Harris, D. L. *Chem. Rev.* **2000**, *100*, 407−419.

(36) Sono, M.; Roach, M. P.; Coulter, E. D.; Dawson, J. H. *Chem. Rev.* **1996**, *96*, 2841−2888.

(37) Hocking, R. K.; Wasinger, E. C.; Yan, Y.-L.; de Groot, F. M. F.; Walker, F. A.; Hodgson, K. O.; Hedman, B.; Solomon, E. I. *J. Am. Chem. Soc.* **2007**, *129*, 113−125.

(38) Wasinger, E. C.; de Groot, F. M. F.; Hedman, B.; Hodgson, K. O.; Solomon, E. I. *J. Am. Chem. Soc.* **2003**, *125*, 12894−12906.

(39) Hocking, R. K.; Wasinger, E. C.; de Groot, F. M. F.; Hodgson, K. O.; Hedman, B.; Solomon, E. I. *J. Am. Chem. Soc.* **2006**, *128*, 10442−10451.

(40) Collman, J. P.; Gagne, R. R.; Reed, C. A.; Robinson, W. T.; Rodley, G. A. *Proc. Natl. Acad. Sci. U.S.A.* **1974**, *71*, 1326−1329.

(41) Collman, J. P. *Acc. Chem. Res.* **1977**, *10*, 265−272.

(42) Scheidt, W. R.; Osvath, S. R.; Lee, Y. J. *J. Am. Chem. Soc.* **1987**, *109*, 1958−1963.

(43) DeBeer George, S.; Metz, M.; Szilagyi, R. K.; Wang, H.; Cramer, S. P.; Lu, Y.; Tolman, W. B.; Hedman, B.; Hodgson, K. O.; Solomon, E. I. *J. Am. Chem. Soc.* **2001**, *123*, 5757−5767.

(44) Yeh, J. J.; Lindau, I. *At. Data Nucl. Data Tables* **1985**, *32*, 1−155.

(45) Hocking, R. K.; DeBeer George, S.; Gross, Z.; Walker, F. A.; Hodgson, K. O.; Hedman, B.; Solomon, E. I. *Inorg. Chem.* **2009**, *48*, 1678−1688.

(46) Dey, A.; Hocking, R. K.; Larsen, P.; Borovik, A. S.; Hodgson, K. O.; Hedman, B.; Solomon, E. I. *J. Am. Chem. Soc.* **2006**, *128*, 9825−9833.

(47) Hocking, R. K.; DeBeer George, S.; Raymond, K. N.; Hodgson, K. O.; Hedman, B.; Solomon, E. I. *J. Am. Chem. Soc.* **2010**, *132*, 4006−4015.

(48) Thole, B. T.; van der Laan, G.; Fuggle, J. C.; Sawatzky, G. A.; Karnatak, R. C.; Esteva, J.-M. *Phys. Rev. B.* **1985**, *32*, 5107−5118.

(49) Cowan, R. D. *The Theory of Atomic Structure and Spectra*; University of California Press: Berkeley, 1981.

(50) Butler, P. H. *Point Group Symmetry: Applications, Methods and Tables*; Plenum Press: New York, 1981.

(51) Arrio, M.-A.; Sainctavit, P.; Cartier dit Moulin, C.; Mallah, T.; Verdaguer, M.; Pellegrin, E.; Chen, C. T. *J. Am. Chem. Soc.* **1996**, *118*, 6422−6427.
(52) van der Laan, G.; Kirkman, I. W. *J. Phys: Condens. Matter* **1992**, *4*, 4189−4204.
(53) Arrio, M.-A.; Scuiller, A.; Sainctavit, P.; Cartier dit Moulin, C.; Mallah, T.; Verdaguer, M. *J. Am. Chem. Soc.* **1999**, *121*, 6414−6420.
(54) Cartier dit Moulin, C.; Villain, F.; Bleuzen, A.; Arrio, M.-A.; Sainctavit, P.; Lomenech, C.; Escax, V.; Baudelet, F.; Dartyge, E.; Gallet, J.-J.; Verdaguer, M. *J. Am. Chem. Soc.* **2000**, *122*, 6653−6658.
(55) Bianconi, A.; Della Longa, S.; Li, C.; Pompa, M.; Congiu-Castellano, A.; Udron, D.; Flank, A. M.; Lagarde, P. *Phys. Rev. B* **1991**, *44*, 10126−10138.
(56) De Groot, F. *Coord. Chem. Rev.* **2005**, *249*, 31−63.
(57) Jianfeng, L.; Nair, S. M.; Noll, B. C.; Schultz, C. E.; Scheidt, W. R. *Inorg. Chem.* **2008**, *47*, 3841.
(58) Jameson, G. B.; Rodley, G. A.; Robinson, W. T.; Gagne, R. R.; Reed, C. A.; Collman, J. P. *Inorg. Chem.* **1978**, *17*, 850−857.
(59) Frisch, M. J.; et al. *Gaussian 09*, Revision B.01; Gaussian Inc.: Wallingford, CT, 2009.
(60) Becke, A. D. *Phys. Rev. A: Gen. Phys.* **1988**, *38*, 3098−3100.
(61) Perdew, J. P. *Phys. Rev. B: Condens. Matter* **1986**, *33*, 8822−8824.
(62) Baerends, E. J.; et al. *ADF2012*; SCM, Theoretical Chemistry, Vrije Universiteit: Amsterdam, The Netherlands, 2012; http://www.scm.com.
(63) Tenderholt, A. L. *QMForge*: A Program to Analyze Quantum Chemistry Calculations, v. 2.1; Stanford University: Stanford, CA, 2007; http://qmforge.sourceforge.net.
(64) Bergman, D. L.; Laaksonen, L.; Laaksonen, A. *J. Mol. Graph. Model.* **1997**, *15*, 301−306.
(65) Laaksonen, L. *J. Mol. Graph.* **1998**, *10*, 33−34.
(66) Jameson, G. B.; Molinaro, F. S.; Ibers, J. A.; Collman, J. P.; Brauman, J. I.; Rose, E.; Suslick, K. S. *J. Am. Chem. Soc.* **1980**, *102*, 3224−3237.
(67) Park, S.-Y.; Yokoyama, T.; Shibayama, N.; Shiro, Y.; Tame, J. R. H. *J. Mol. Biol.* **2006**, *360*, 690−701.
(68) Vojtěchovský, J.; Chu, K.; Berendzen, J.; Sweet, R. M.; Schlichting, I. *Biophys. J.* **1999**, *77*, 2153−2174.